Nanocomposites of graphene oxide, Ag nanoparticles, and magnetic ferrite nanoparticles for elemental mercury (Hg0) removal

Liu, Yuxi; Tian, Chong; Yan, Bin; Lu, Qingye; Xie, Yijun; Chen, Jian; Gupta, Rajender; Xu, Zhenghe; Kuznicki, Steven M.; Liu, Qingxia; Zeng, Hongbo

Publisher's version / Version de l'éditeur:
https://doi.org/10.1039/C4RA16016A
RSC Advances, 5, 20, pp. 15634-15640, 2015-01-27

RSC Advances

PAPER

View Article Online
View Journal | View Issue

Cite this: *RSC Adv.*, 2015, **5**, 15634

Nanocomposites of graphene oxide, Ag nanoparticles, and magnetic ferrite nanoparticles for elemental mercury (Hg^0) removal†

Yuxi Liu,[a] Chong Tian,[ab] Bin Yan,[a] Qingye Lu,[a] Yijun Xie,[a] Jian Chen,[c] Rajender Gupta,[a] Zhenghe Xu,[a] Steven M. Kuznicki,[a] Qingxia Liu[a] and Hongbo Zeng*[a]

Mercury emission from combustion flue gas causes considerable environmental challenges and serious adverse health threats, and elemental mercury (Hg^0) is the most challenging chemical form for removal. In this work, four types of graphene oxide (GO) based composite adsorbents were successfully synthesized by depositing Ag nanoparticles (NPs) and/or magnetic ferrite NPs on GO sheets (denoted as GO, GO–Ag, MGO and MGO–Ag), characterized and applied for the removal of Hg^0 for the first time. The presence of Ag NPs on GO greatly enhances the Hg^0 removal capability of GO–Ag and MGO–Ag as compared to that of pure GO, which is mainly attributed to the amalgamation of Hg^0 on Ag NPs. MGO–Ag shows the best Hg^0 removal performance and thermal tolerance among the four types of adsorbents developed, which can effectively capture Hg^0 up to 150–200 °C in a simulated flue gas environment and can be also effectively recycled and reused. Our results indicate that the graphene oxide based composites (*i.e.* MGO–Ag) have significant potential applications for mercury emission control in coal-fired power plants.

Received 9th December 2014
Accepted 27th January 2015

DOI: 10.1039/c4ra16016a

www.rsc.org/advances

1. Introduction

As one of the most abundant fossil fuels, coal is the dominant energy source for production of electricity and heat through coal-fired power plants worldwide. Coal combustion causes considerable environmental challenges and serious health threats by emissions of particulate matter (<10 μm) and toxic trace elements (especially mercury).[1–3] Mercury finds its way out in emissions through precipitation and bioaccumulation, which results in serious health problems.[4,5] Mercury presents as three major chemical forms in combustion flue gases: elemental (Hg^0), particulate-bound (Hg_p) and oxidized (Hg^{2+}) forms.[6–9] Hg^{2+} and Hg_p can be relatively easily eliminated by air pollution control devices (APCDs), while Hg^0 is much more difficult to remove due to its high equilibrium vapor pressure and low water solubility.[7,10–12] Generally, a considerable proportion (20–85%) of Hg^0 remained in the flue gases released from post-treatment systems,[9] resulting in an intractable challenge for Hg^0 removal.

Much effort has been devoted to the development of efficient adsorbents to remove mercury from combustion flue gases. Efficient adsorbents typically require large specific surface area which ensures sufficient contact between adsorbents and mercury, and high degree of surface reactivity for a suitable mercury adsorption capacity. Therefore, porous materials[13–17] such as activated carbons, zeolite, and mesoporous silica have been extensively explored as scaffolds to impregnate active chemicals including chlorine, sulfur, bromide, iodine and noble metals, and are employed as adsorbents.[13,18,19] However, most of these sorbents are difficult to regenerate due to the strong chemical interactions involved in mercury adsorption, thereby incurring high operating costs. It is of paramount benefit to explore a novel scaffold and develop efficient mercury adsorbents with feasible recycling ability under suitable regeneration temperature, which will not only greatly enhance the mercury removal performance but also significantly reduce the operation cost of sorbent injection.

Graphene oxide (GO) derived from graphene has received much attention over the past few years as a novel adsorbent substrate for various applications due to its outstanding features,[20] such as large specific surface area, high water dispersibility, and good surface functionalization feasibility. Taking advantage of the abundant functional groups and large surface areas, various functionalized GO composites, such as polypyrrole-reduced GO (RGO), RGO–MnO_2, RGO–Ag and

[a]*Department of Chemical and Material Engineering, University of Alberta, Edmonton, AB, T6G 2V4, Canada. E-mail: Hongbo.Zeng@ualberta.ca; Fax: +1-780-492-2881; Tel: +1-780-492-1044*

[b]*State Key Laboratory of Coal Combustion, Huazhong University of Science and Technology, Wuhan 430074, P. R. China*

[c]*National Institute for Nanotechnology, National Research Council, Edmonton, Alberta, T6G 2M9, Canada*

† Electronic supplementary information (ESI) available: Additional FE-SEM images, TEM images, TEM-EDX spectra, XPS spectra, TGA analysis, and mercury adsorption results of the GO based composites, and experiment setup for mercury breakthrough test. See DOI: 10.1039/c4ra16016a

RGO–SnO_2 composites, have been developed for removal of Hg^{2+} in water treatment and detection of Hg^{2+}.[21,22] Metal and metal oxide nanoparticles were among the most intensively studied Hg^0 adsorbents in previous studies.[23–25] In particular, noble metal nanoparticles, such as silver and gold, are the most intriguing ones,[20,24,26,27] which can efficiently capture mercury vapour by forming Ag–Hg or Au–Hg amalgam at temperatures close to flue gas conditions and can be regenerated by release of captured mercury through thermal treatment, providing a feasible way to regenerate mercury adsorbents. Meanwhile, surface functional groups (*e.g.* hydroxyl, epoxy, carboxyl) on adsorbents have been reported as active sites for Hg^0 adsorption.[28] Thus, GO composites decorated with noble metal nanoparticles are expected to have great potential in mercury removal from coal flue gases. Yet, to date, no study has been reported on GO based composites for removal of elemental mercury from flue gases.

Herein, we applied GO, for the first time, as a scaffold for developing a regenerable mercury sorbent. By incorporating silver and magnetic nanoparticles on GO surfaces, GO and several GO based composites including magnetic nanoparticle–GO (MGO), silver nanoparticle–GO (GO–Ag), and MGO–Ag were synthesized, characterized and applied to remove Hg^0 under various temperatures. The recyclability of MGO–Ag was investigated and its Hg^0 adsorption capacity was also explored in simulated combustion gases.

2. Experiment section

2.1. Materials

Graphite flakes with a median of 7–10 micron, sulfuric acid (H_2SO_4, 95.0–98.0 wt%), sodium nitrate ($NaNO_3$, 99.0%), hydrogen peroxide (H_2O_2, 29–32% w/w aq.) and poly(*N*-vinyl-2-pyrrolidone) (PVP, average M.W. 58 000) were purchased from Alfa Aesar. α-D-Glucose (96%), iron(III) chloride hexahydrate ($FeCl_3 \cdot 6H_2O$, 99.0%) and iron(II) chloride tetrahydrate ($FeCl_2 \cdot 4H_2O$, 99.0%) were supplied by Sigma-Aldrich. Potassium permanganate ($KMnO_4$, 99.0%), ammonia solution (29.5 wt%) and silver nitrate ($AgNO_3$, 99.7%) were provided by Fisher Scientific.

2.2. Synthesis of GO

GO was prepared according to the Hummer's method.[29] Firstly, H_2SO_4 (98 wt%, 150 mL) was added to a three-neck flask with graphite powder (2 g) and $NaNO_3$ (1.5 g) in an ice bath. Then $KMnO_4$ (9.1 g) was gradually added and vigorously stirred for 5 days. Afterwards, H_2O_2 (30 wt%, 6 mL) was added, and the resulted solution was slowly diluted with a mixture of 500 mL deionization (DI) water, H_2SO_4 (98%, 15 mL) and H_2O_2 (30 wt%, 8.35 mL) while the color of the suspension would change to brilliant yellow. Then, the resultant was centrifuged and washed several times with DI water, followed by dialysis against 2 L DI water with water exchange every 4 hours for 2 days. Finally, loose brownish black powders were obtained after freeze drying.

2.3. Synthesis of GO–Ag

GO–Ag composites were synthesized according to a revised procedure based on a previous report[30] and briefly described as follows: a homogeneous aqueous mixture of GO (0.5 mg mL^{-1}, 100 mL) was obtained after 45 min ultrasonical exfoliation. Then, PVP solution (4 mg mL^{-1}, 20 mL) and glucose (1.6 g) were added sequentially under vigorous stirring. A silver–ammonia aqueous solution (18.7 mg mL^{-1}, 20 mL) was added to the above mixture at 60 °C, and the reaction was held at this temperature for 7 min. Finally, GO–Ag composites were collected by centrifuging and purified with thoroughly washing with ethanol and DI water for several times. Followed by freeze drying, the dry GO–Ag composites were reclaimed as grey black powders.

2.4. Synthesis of MGO and MGO–Ag

MGO composites were synthesized following a modified procedure based on a recent report[31] and the details were shown as follows. An aqueous solution of $FeCl_3$ and $FeCl_2$ in 2 : 1 mole ratio was added to a homogenous aqueous solution of GO (5 mg mL^{-1}, 50 mL) prepared *via* 45 min ultrasonication treatment at room temperature. The whole system was heated to 90 °C, and pH of the mixture was adjusted to 10 by using 30 wt% ammonia solution. After being vigorously stirred for 40 min, the solution was cooled down to room temperature. The resulting black composites were collected by a magnet and washed thoroughly with copious amount of DI water and then reclaimed by freeze drying, and the final product was denoted as MGO. MGO–Ag was synthesized by the same procedure as that for GO–Ag with MGO as the initial reactant.

2.5. Material characterizations

The morphologies of the as-prepared GO and GO–nanoparticle composites were characterized by field emission-scanning electron microscopy (FE-SEM) using a JAMP-9500F (Jeol, Japan), transmission electron microscopy (TEM) using a Philips/FEI Morgagni microscope at 80 kV and a JEOL JEM-2200FS TEM operated at 200 kV. The element compositions of all composites were analyzed by X-ray diffraction (XRD) on a Rigaku Ultima IV X-ray diffractometer using Cu Kα irradiation ($k = 1.5406$ Å) and X-ray photoelectron spectroscopy (XPS) on an AXIS 165 spectrometer (Kratos Analytical). Magnetic hysteresis measurements were performed on a Quantum Design 9T-PPMS magnetometer at 300 K under an applied field of 5000 Oe. Thermal gravimetric analysis (TGA) was conducted on a TA instrument SDT Q600 to measure the thermal properties of GO.

2.6. Mercury breakthrough test

The mercury breakthrough experiments were carried out by using a Tekran 2500 Cold Vapor Atomic Fluorescence Spectrophotometer (CVAFS).[24] The details about CVAFS measurement setup are given in Scheme S1 (ESI†). 15 mg GO based adsorbents were precisely weighed and loaded into a borosilicate glass u-tube with an inner diameter of 4 mm, held into a GC oven which was used to control the temperature for the adsorbents to capture Hg^0. 200 μL of Hg^0 standard vapor at room

temperature was injected into the system with an argon flow rate of 40 mL min^{-1} and exposed to loaded adsorbent in each test. A GB trap filled with gold beads (GB) and wrapped with a heating wire was applied to capture the Hg^0 escaped from the upstream adsorbent and would be heated later to release the Hg^0 to a downstream Hg^0 detector-CVAFS. The mercury breakthrough value was correspondingly calculated as the ratio between the amount of Hg^0 that has not been captured by the loaded composite adsorbent under designed experimental conditions and the total amount of Hg^0 injected.

3. Results and discussions

3.1. Characterizations of the developed GO–nanoparticle composites

The morphologies of the as-prepared GO, GO–Ag, MGO and MGO–Ag were characterized by FE-SEM, TEM and high resolution TEM (HRTEM). The FE-SEM and TEM images of GO (Fig. 1a and S1e in ESI†) show a typical morphology of thin sheets with some wrinkles that is consistent with previous reports.[32,33] A relatively uniform distribution of Ag NPs with an average particle size of 50 nm on GO surfaces can be observed and shown in the FE-SEM (Fig. 1b) and TEM images of GO–Ag (Fig. 1c). It should be noted that by tuning the initial concentration of $[Ag(NH_3)_2]OH$ added, GO–Ag composites with different silver loadings could be easily achieved (see Fig. S1a and S1b in ESI†) while would not lead to significant size variation of the Ag NPs deposited. Fig. 1d and e show the HRTEM images of as-prepared MGO–Ag which exhibit massive ultra-fine magnetic nanoparticles around 10 nm dispersed with Ag NPs on GO substrates. Possible deposition mechanism of Ag and iron oxides NPs involves first-stage electrostatic adsorption of Ag, Fe ions on the negatively charged GO surfaces (*e.g. via* oxygen-containing functional groups) and second-stage *in situ* reduction of the ions as well as crystallization of the Ag and iron oxides NPs.[30–32] The Fast Fourier Transformation (FFT) pattern (Fig. 1e) of selected nanoparticles highlighted in the red rectangular region of Fig. 1d displays a 0.24 nm interfringe distance of Ag that could be assigned to the (1 1 1) crystallographic plane of face centered cubic (fcc) Ag and a 0.29 nm interfringe distance of the iron oxides that could be assigned to the (2 2 0) crystallographic plane of face centered cubic (fcc) Fe. The above results indicate the successful deposition of both Ag and magnetic NPs on GO surfaces, as further confirmed by HRTEM image coupled with energy dispersive X-ray spectroscopy (HRTEM-EDX) showing a homogeneous and dense mapping of Fe and Ag elements on GO sheets in Fig. 1f.

To further verify the successful synthesis of the GO composites and characterize the compositions of the NPs, XRD and XPS analyses was conducted. The XRD patterns of GO, GO–Ag, GO–1/2Ag, GO–1/4Ag, MGO and MGO–Ag are shown in Fig. 2a. GO exhibits a clear diffraction peak at 9.92°, indicating an expanded GO interlayer spacing of 0.89 nm calculated from Bragg equation. Compared with the ~0.34 nm *d*-spacing of the pristine graphite, the *d*-spacing of GO is much larger due to the addition of surface oxygen-containing functional groups.[33,34] Comparing the XRD spectra of GO and GO–nanoparticle

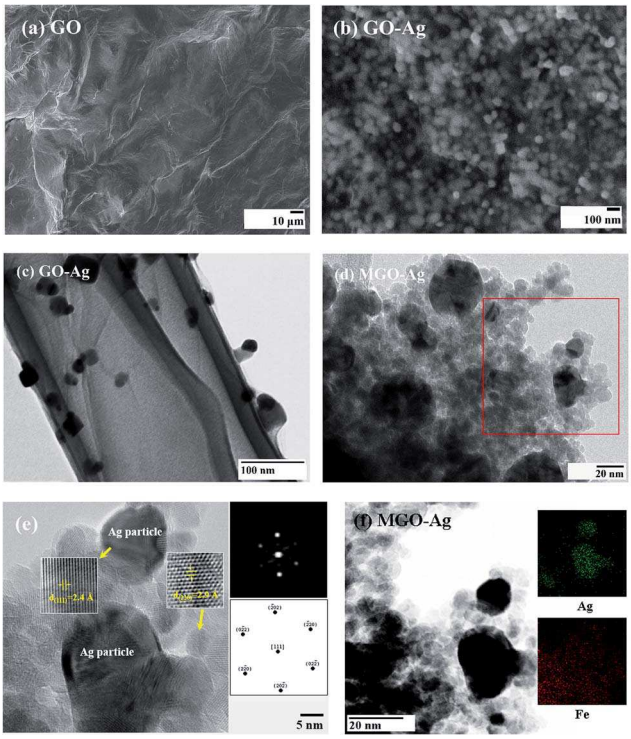

Fig. 1 FE-SEM images of (a) GO, (b) GO–Ag. (c) TEM image of GO–Ag. HRTEM images of (d) MGO–Ag and (e) selected nanoparticles of MGO–Ag. The inset is the FFT pattern (image after Wiener Filter processing and the diffractogram) of the same enlarged iron oxide particle. The FFT index suggests this iron oxide particle is Fe_2O_3. (f) HRTEM-EDX spectra of Fe, Ag on MGO–Ag enclosed by the red rectangular area in (d).

composites, a typical diffraction peak for GO at 9.92° was absent in the GO–nanoparticle composites, revealing further exfoliation of GO sheets by ultrasonication,[34] which leads to the effective dispersion of Ag NPs and magnetic NPs during synthesis. The diffraction peaks shown in the XRD spectra of GO–Ag and MGO–Ag at $2\theta = 38.2°$, 44.3°, 64.5°, 77.5° and 81.6° can be assigned to (1 1 1), (2 0 0), (2 2 0), (3 1 1) and (2 2 2) crystallographic planes of silver nanoparticles (in good agreement with no. 04-0783 JCPDS Card), indicating the successful deposition of Ag NPs on GO surfaces. In addition, the XRD data of MGO and MGO–Ag displays the diffraction peaks originating from both cubic Fe_3O_4 (JCPDS Card no. 75-0449) and cubic γ-Fe_2O_3 (JCPDS Card no. 39-1346), indicating that the co-precipitation method results in simultaneous formation of Fe_3O_4 and γ-Fe_2O_3 on GO surfaces.

The XPS spectra of all the synthesized composites are shown in Fig. S2a (ESI†) which display the major element peaks of C1s, O1s, Ag 3d and Fe 2p. The C1s XPS spectrum of GO (Fig. 2b) can be fitted with five curves located at 284.6 eV (C=C/C–C), 285.5 eV (C–OH), 286.9 eV (C–O–C), 287.8 eV (C=O) and 288.9 eV (COOH), respectively, confirming the successful synthesis of GO. The C1s XPS spectra of the GO–nanoparticle composites with similar peaks are shown in Fig. S2b–f (ESI†). After the deposition of silver and magnetic nanoparticles, sharp XPS peaks at 368.2 eV and at 374.2 eV assigned to Ag $3d_{5/2}$ and

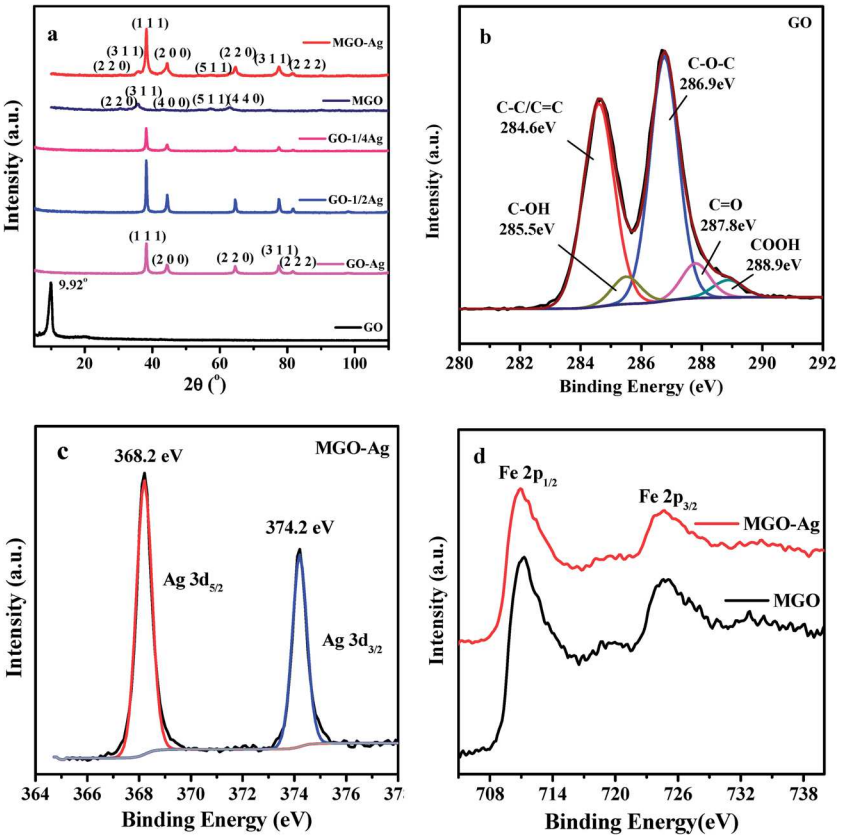

Fig. 2 (a) XRD spectra of GO, GO–Ag, GO–1/2Ag, GO–1/4Ag, MGO and MGO–Ag composites. XPS survey scans of (b) C on GO, (c) Ag on MGO–Ag and (d) Fe on MGO and MGO–Ag.

Ag $3d_{3/2}$ were clearly detected on GO–Ag and MGO–Ag composites, which are in accordance with the reported binding energy of metallic silver.[35,36] Furthermore, a small satellite peak of Fe $2p_{3/2}$ at ~718 eV appears on the Fe XPS spectra (Fig. 2d) of both MGO and MGO–Ag, indicating the coexistence of γ-Fe_2O_3 and cubic Fe_3O_4 on GO surfaces (consistent with XRD measurements in Fig. 2a).[37] The loading percentages (atomic number ratio) of Ag and Fe on MGO–Ag as detected by XPS are 3.39% and 4.27%, respectively. All the above results demonstrate the successful synthesis of GO–nanoparticle composites.

In order to test the possibility of recycling the developed MGO and MGO–Ag composites *via* applying an external magnetic field, the magnetism of the as-prepared MGO and MGO–Ag was evaluated by magnetic hysteresis loop measurements. As shown in Fig. 3, both MGO and MGO–Ag show typical superparamagnetism with no hysteresis loops, which guarantees the convenient reclamation of MGO and MGO–Ag composites after mercury adsorption and re-dispersion of these composites *via* withdrawal of the magnetic field for recycling. Saturation magnetizations of 14.9 emu g^{-1} and 13.4 emu g^{-1} were measured for MGO–Ag and MGO, respectively, which are comparable to that of ultrafine magnetic nanoparticles reported previously[38,39] and strong enough for easy separation of the MGO and MGO–Ag composites (see inset graph in Fig. 3). It should be noted that a slightly higher saturation magnetization was obtained for MGO–Ag than that of MGO, which is most likely attributed to the magnetic moment change induced by the dipolar interactions between ferrite and Ag nanoparticles.[40]

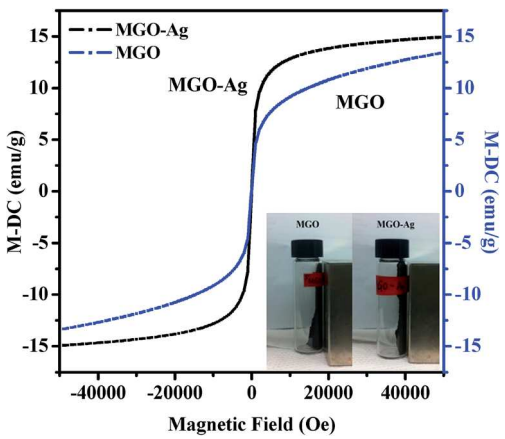

Fig. 3 Magnetization curves of MGO and MGO–Ag. The inset photographs: separation of MGO and MGO–Ag by a magnet.

3.2. Mercury adsorption of GO–nanoparticle composites

To investigate the Hg^0 adsorption capability of the developed GO composites including GO, GO–Ag, MGO and MGO–Ag, the mercury breakthrough was examined over a wide temperature range from 50 °C to 250 °C. As shown in Fig. 4, GO displays a

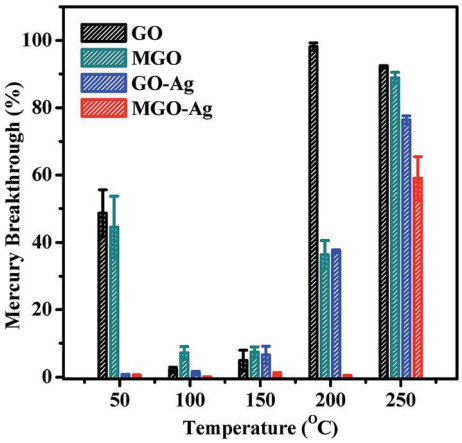

Fig. 4 Mercury breakthrough at different temperatures on various composite materials: GO, GO–Ag, MGO and MGO–Ag.

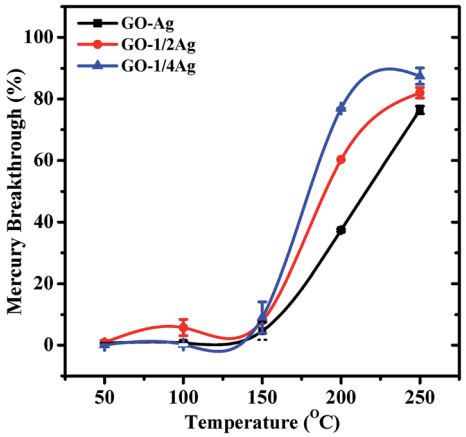

Fig. 5 Mercury breakthrough at different temperatures for GO–Ag, GO–1/2Ag, and GO–1/4Ag.

mercury breakthrough of 50% at low temperature (*i.e.* 50 °C) and an excellent mercury capturing performance with the nearly complete mercury capture at the tested temperatures of 100 °C and 150 °C, but the Hg^0 adsorption capabilities were totally deteriorated once the temperature reached above 200 °C. Previous study showed that surface moisture and low temperature could significantly lower the adsorption capability of Hg^0 on AC,[41] which most likely leads to the low mercury removal (~50%) of GO at 50 °C observed here. The high Hg^0 adsorption capability of GO at 100–150 °C is probably attributed to abundant surface functional groups (*e.g.* hydroxyl, epoxy, carboxyl) on GO surfaces, which have been demonstrated as active sites for Hg^0 adsorption.[28] To test the above hypothesis, a control experiment was carried out: GO was exposed to thermal treatment at 350 °C to remove all the functional groups (as verified by TGA measurement shown in Fig. S4, ESI†), and the treated GO was then applied for mercury breakthrough measurement. It was found that GO composites lost the Hg^0 adsorption capability after thermal treatment at 350 °C (Fig. S5, ESI†), thereby supporting that functional groups on GO determine its Hg^0 adsorption performance. Hence, it might be challenging to regenerate GO composites after releasing Hg^0 *via* a thermal treatment at high temperature. However, compared to the conventional widely-applied carbon based adsorbents with a very weak adsorption of Hg^0 above 50 °C (<20% under similar experimental conditions to the current work, and further losing Hg^0 adsorption capability at higher temperature),[19] GO composites are expected to still bear great advantages as activated adsorbent for Hg^0 removal in coal combustion flue gas, particularly with the addition of Ag nanoparticles and magnetic nanoparticles.

As shown in Fig. 4, with the incorporation of Ag NPs, the as-prepared GO–Ag composites exhibit enhanced Hg^0 adsorption capability as compared to that of GO as evident from the lower mercury breakthrough, especially at high temperatures, which is mainly due to a stable Ag–Hg amalgam formed.[18,19,24,25] The Hg^0 adsorption capability of GO–Ag could be further enhanced by increasing the silver content loaded on GO surfaces. The results in Fig. 5 clearly demonstrate that increasing Ag loading on GO–Ag composites strengthens their Hg^0 adsorption capability as evident from the low mercury breakthrough at 150–250 °C, *i.e.*, Hg^0 breakthrough of GO–Ag < GO–1/2Ag < GO–1/4Ag. Because mercury could be reversibly released from Ag–Hg amalgam, the GO–Ag composites could be easily regenerated after a thermal treatment at a high temperature. As shown in Fig. S6 (ESI†), unlike GO composites, GO–Ag composites could nearly fully recover its Hg^0 adsorption capability after thermal treatment at 350 °C, indicating that the GO–Ag based composites are highly regenerable.

In order to confer the feasible reclamation ability of the GO–Ag composites during recycling, magnetic nanoparticles were introduced onto the GO composites, which allows the MGO–Ag to be easily separated under an external magnetic field (as shown in Fig. 3). The impact of the addition of magnetic nanoparticles on the Hg^0 adsorption capability of MGO and MGO–Ag composites was shown in Fig. 4. Overall, the incorporation of magnetic nanoparticles does not weaken the Hg^0 adsorption capability of MGO composites as compared to that of GO over the whole temperature range studied (50–250 °C). The further addition of Ag NPs significantly enhanced the Hg^0 adsorption capability of MGO–Ag, which shows the best Hg^0 removal performance among all the four composites (*i.e.* GO, GO–Ag, MGO, and MGO–Ag) particularly at high temperature (150–250 °C) as shown in Fig. 4, indicating the best tolerance at high temperature. It is believed that physisorption and Ag–Hg amalgamation play important roles in the adsorption of Hg^0 on the GO based adsorbents,[19,24] and all the four composites show weakened Hg^0 adsorption capability at 250 °C, which provides a feasible method for recycling the adsorbent materials (as discussed later). The above results also indicate that the deposition of both Ag NPs and magnetic iron oxide NPs on GO could synergistically enhance the Hg^0 capturing capability and temperature tolerance of the MGO–Ag composites as compared to the other three adsorbents, which shows significant potential for the removal of Hg^0 from flue gases. This synergic performance is most likely achieved through Ag–Hg amalgamation coupled with chemi-sorption and amalgamation of Hg^0 on ferrite oxide NPs as reported previously.[13,25,42]

To explore the recyclability of MGO–Ag, the mercury breakthrough recycling test was carried out at 200 °C, and the regeneration of the MGO–Ag composite was achieved by thermal treatment at 370 °C as detected by CVAFS. Fig. 6 shows that MGO–Ag could maintain almost 100% of the Hg^0 adsorption capability (equivalent to almost 0% breakthrough) even after 5 cycles of reuse. Meanwhile, the TEM, TEM-EDX and XPS results of the MGO–Ag composites after recycling test (see Fig. 7 and S7 in ESI†) show that the composites maintain their physical and chemical structures after recycling, demonstrating excellent stability. The above results further demonstrate that the MGO–Ag composites could be regenerated after a thermal treatment at high temperature without significant destruction of MGO–Ag and deterioration of Hg^0 adsorption capability, suggesting that the as-prepared MGO–Ag has great potential application in Hg^0 removal from practical flue gases.

The Hg^0 adsorption capacity of MGO–Ag was further tested by continuous exposure to simulated flue gases (consisted of 4% O_2, 12% CO_2, 400 ppm SO_2, 300 ppm NO and 75 μg m^{-3} Hg^0 that is two times higher than the Hg^0 concentration in real flue gases[43,44]) at a flow rate of 1.2 L min^{-1} for 0.5 h to explore its potential practical mercury removal capability in coal combustion flue gases, and the inlet and outlet Hg^0 concentrations of the gas flow were monitored by a VM-3000 Mercury Vapour Detector. Fig. 8 shows that MGO–Ag exhibits Hg^0 capture capacity of about 60 μg g^{-1} (w/w, adsorbed Hg^0/adsorbent) at 100 to 150 °C, which is much higher than Hg^0 capture capacity of previously reported adsorbents such as fly ash (10–30 μg g^{-1} at 135 °C)[45] and magnetic zeolite silver composites (13.3–40 μg g^{-1} at 150 °C)[18] under similar experimental conditions. Furthermore, it demonstrates a faster Hg^0 adsorption rate in the simulated flue gases: ~4.5 ppm Hg^0 (w/w, Fig. S8 in ESI†) was captured by 15 mg MGO–Ag in the first 5 min over the whole temperature range (100–200 °C), which outperforms the previously reported Ag NPs based composites within the same exposure time (~140 ppb of chabazite-based Ag composite and ~30 ppb of magnetic zeolite silver composite).[24,46] It is also noted that the Hg^0 capture capacity of MGO–Ag dramatically drops to ~7 μg g^{-1} as the temperature of simulated flue gases increases to 200 °C. All the above results indicate that the MGO–Ag composites could be used as potential adsorbents for mercury emission control in the practical downstream flue gas (typically with a temperature of 100–150 °C) of coal-fired power plant.[43]

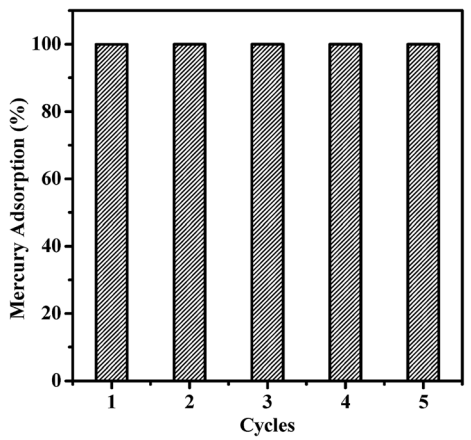

Fig. 6 Hg^0 adsorption recycling tests for regenerated MGO–Ag at 200 °C.

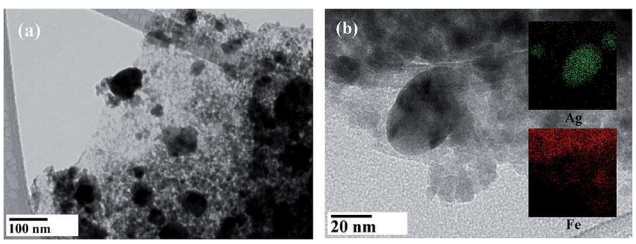

Fig. 7 (a) TEM image of MGO–Ag after recycling test. (b) HRTEM image of MGO–Ag after recycling test with EDX spectra (insets).

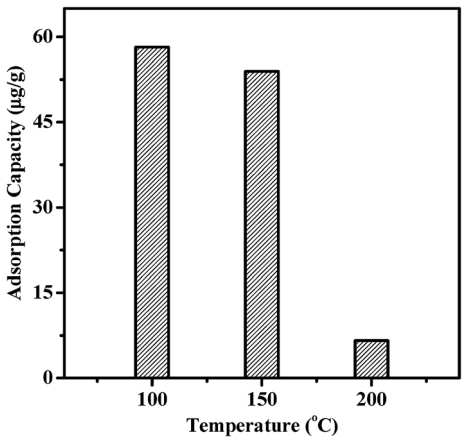

Fig. 8 The Hg^0 adsorption capacity of MGO–Ag under continuous exposure to simulated flue gases for 0.5 h from 100 °C to 200 °C.

4. Conclusions

In this work, four types of novel adsorbents based on graphene oxide composites (*i.e.* GO, GO–Ag, MGO and MGO–Ag) were successfully synthesized, characterized and applied for the adsorption of elemental mercury (Hg^0) for the first time. The deposition of Ag NPs on GO enhances the Hg^0 removal capability of GO–Ag as compared to that of pure GO, mainly due to amalgamation between Ag NPs and Hg^0. The addition of magnetic ferrite NPs on GO does not show a negative impact on the Hg^0 removal capability of MGO. The deposition of both Ag NPs and magnetic NPs on GO makes the MGO–Ag composites possess the best Hg^0 removal capability and thermal tolerance among the four types of adsorbents tested. MGO–Ag composites are able to effectively capture Hg^0 up to 150–200 °C in simulated flue gas environment, which can be also effectively recycled and reused with excellent thermal stability. Our results indicate that the graphene oxide based composites (*i.e.* MGO–Ag) have significant potential applications for mercury emission control in coal-fired power plant.

Acknowledgements

The authors are grateful for the financial support from the Helmholtz-Alberta Initiative – Energy & Environment (HAI-E&E) program and Natural Sciences and Engineering Research Council of Canada (NSERC).

References

1 Environmental Impacts of Coal Power: Air Pollution, http://www.ucsusa.org/clean_energy/coalvswind/c02c.html, accessed October.
2 C. L. Carlson and D. C. Adriano, *J. Environ. Qual.*, 1993, **22**, 227–247.
3 R. B. Finkelman, W. Orem, V. Castranova, C. A. Tatu, H. E. Belkin, B. Zheng, H. E. Lerch, S. V. Maharaj and A. L. Bates, *Int. J. Coal Geol.*, 2002, **50**, 425–443.
4 W. F. Fitzgerald, *Water, Air, Soil Pollut.*, 1995, **80**, 245–254.
5 A. P. Dastoor and Y. Larocque, *Atmos. Environ.*, 2004, **38**, 147–161.
6 K. C. Z. Galbreath and C. J. Zygarlicke, *Environ. Sci. Technol.*, 1996, **30**, 2421–2426.
7 K. C. Galbreath and C. J. Zygarlicke, *Fuel Process. Technol.*, 2000, **65–66**, 289–310.
8 J. H. Pavlish, E. A. Sondreal, M. D. Mann, E. S. Olson, K. C. Galbreath, D. L. Laudal and S. A. Benson, *Fuel Process. Technol.*, 2003, **82**, 89–165.
9 H. Yang, Z. Xu, M. Fan, A. E. Bland and R. R. Judkins, *J. Hazard. Mater.*, 2007, **146**, 1–11.
10 O. Lindqvist, K. Johansson, M. Aastrup, A. Anderson, L. Bringmark and G. Hovsenius, *Water, Air, Soil Pollut.*, 1991, **55**, 1–261.
11 Y. Liu, T. M. Bisson, H. Yang and Z. Xu, *Fuel Process. Technol.*, 2010, **91**, 1175–1197.
12 B. M. Reddy, N. Durgasri, T. V. Kumar and S. K. Bhargava, *Catal. Rev.: Sci. Eng.*, 2012, **54**, 344–398.
13 E. J. Granite, H. W. Pennline and R. A. Hargis, *Ind. Eng. Chem. Res.*, 2000, **39**, 1020–1029.
14 H. Zeng, F. Jin and J. Guo, *Fuel*, 2004, **83**, 143–146.
15 M. A. Abu-Daabes and N. G. Pinto, *Chem. Eng. Sci.*, 2005, **60**, 1901–1910.
16 P. Worathanakul, P. Kongkachuichay, J. D. Noel, A. Suriyawong, D. E. Giammar and P. Biswas, *Environ. Eng. Sci.*, 2008, **25**, 1061–1070.
17 Y. Xie, B. Yan, H. Xu, J. Chen, Q. Liu, Y. Deng and H. Zeng, *ACS Appl. Mater. Interfaces*, 2014, **6**, 8845–8852.
18 J. Dong, Z. Xu and S. M. Kuznicki, *Adv. Funct. Mater.*, 2009, **19**, 1268–1275.
19 G. Luo, H. Yao, M. Xu, X. Cui, W. Chen, R. Gupta and Z. Xu, *Energy Fuels*, 2010, **24**, 419–426.
20 Y. Zhu, S. Murali, W. Cai, X. Li, J. W. Suk, J. R. Potts and R. S. Ruoff, *Adv. Mater.*, 2010, **22**, 3906–3924.
21 V. Chandra and K. S. Kim, *Chem. Commun.*, 2011, **47**, 3942.
22 T. S. Sreeprasad, S. M. Maliyekkal, K. P. Lisha and T. Pradeep, *J. Hazard. Mater.*, 2011, **186**, 921–931.
23 S. Poulston, E. J. Granite, H. W. Pennline, C. R. Myers, D. P. Stanko, H. Hamilton, L. Rowsell, A. W. J. Smith, T. Ilkenhans and W. Chu, *Fuel*, 2007, **86**, 2201–2203.
24 Y. Liu, D. J. A. Kelly, H. Yang, C. C. H. Lin, S. M. Kuznicki and Z. Xu, *Environ. Sci. Technol.*, 2008, **42**, 6205–6210.
25 J. Wilcox, E. Rupp, S. C. Ying, D.-H. Lim, A. S. Negreira, A. Kirchofer, F. Feng and K. Lee, *Int. J. Coal Geol.*, 2012, **90–91**, 4–20.
26 T. Y. Yan, *Ind. Eng. Chem. Res.*, 1994, **33**, 3010–3014.
27 Y. Xie, B. Yan, C. Tian, Y. Liu, Q. Liu and H. Zeng, *J. Mater. Chem. A*, 2014, **2**, 17730–17734.
28 Y. H. Li, C. W. Lee and B. K. Gullett, *Fuel*, 2003, **82**, 451–457.
29 J. Shen, Y. Hu, M. Shi, N. Li, H. Ma and M. Ye, *J. Phys. Chem. C*, 2010, **114**, 1498–1503.
30 X.-Z. Tang, X. Li, Z. Cao, J. Yang, H. Wang, X. Pu and Z.-Z. Yu, *Carbon*, 2013, **59**, 93–99.
31 M. Z. Kassaee, E. Motamedi and M. Majdi, *Chem. Eng. J.*, 2011, **172**, 540–549.
32 C. Hou, Q. Zhang, M. Zhu, Y. Li and H. Wang, *Carbon*, 2011, **49**, 47–53.
33 Y. Fu, J. Wang, Q. Liu and H. Zeng, *Carbon*, 2014, **77**, 710–721.
34 L. Liu, J. Liu, Y. Wang, X. Yan and D. D. Sun, *New J. Chem.*, 2011, **35**, 1418.
35 J. F. Weaver and G. B. Hoflund, *Chem. Mater.*, 1994, **6**, 1693–1699.
36 K. Heister, M. Zharnikov and M. Grunze, *J. Phys. Chem. B*, 2001, **105**, 4058–4061.
37 T. Yamashita and P. Hayes, *Appl. Surf. Sci.*, 2008, **254**, 2441–2449.
38 D. H. Han, J. P. Wang and H. L. Luo, *J. Magn. Magn. Mater.*, 1994, **136**, 176–182.
39 Z. Ai, K. Deng, Q. Wan, L. Zhang and S. Lee, *J. Phys. Chem. C*, 2010, **114**, 6237–6242.
40 C. H. Liu, Z. D. Zhou, X. Yu, B. Q. Lv, J. F. Mao and D. Xiao, *Inorg. Mater.*, 2008, **44**, 291–295.
41 Y. H. Li, C. W. Lee and B. K. Gullett, *Carbon*, 2002, **40**, 65–72.
42 S. Wu, N. Oya, M. Ozaki, J. Kawakami, M. A. Uddin and E. Sasaoka, *Fuel*, 2007, **86**, 2857–2863.
43 R. Meij, *Water, Air, Soil Pollut.*, 1991, **56**, 21–33.
44 N. Pirrone, S. Cinnirella, X. Feng, R. B. Finkelman, H. R. Friedli, J. Leaner, R. Mason, A. B. Mukherjee, G. B. Stracher, D. G. Streets and K. Telmer, *Atmos. Chem. Phys.*, 2010, **10**, 5951–5964.
45 T. R. Carey and C. F. Richardson, *Environ. Prog.*, 2004, **19**, 167–174.
46 J. Dong, Z. Xu and S. M. Kuznicki, *Adv. Funct. Mater.*, 2009, **19**, 1268–1275.

